Spatiotemporal Adaptation Algorithm for Two-Dimensional Reacting Flows

Mehtab M. Pervaiz* and Judson R. Baron†
Massachusetts Institute of Technology, Cambridge, Massachusetts

A spatiotemporal adaptive algorithm for solving the unsteady Euler equations with chemical source terms is presented. Quadrilateral cells are used in two spatial dimensions that allow for embedded meshes tracking moving flow features with spatially varying time steps which are multiples of global minimum time steps. Blast wave interactions corresponding to a perfect gas and a Lighthill dissociating gas (nonequilibrium) are considered for a circular arc cascade geometry.

Introduction

THE coupling between fluid flow and finite-rate chemistry can introduce appreciable stiffness in numerical schemes, which then involve prohibitively long computation times. Typically, fine *spatial* resolution is desired in the regions characterized by steep changes. Similarly, fine *temporal* resolution is needed when nonequilibrium source terms imply large temporal gradients and also in regions of spatially fine cells due to coupling of time steps with cell volumes.

The use of locally refined spatial grids for steady flow situations has been well demonstrated.[1-5] For such situations, the convergence can be accelerated by using local time stepping and multiple-grid techniques. For unsteady flows, such techniques are inapt; a scheme is introduced here that allows for spatial variation of time steps which are integral multiples of global minimum time step. This *time-stride* approach involves multiple integration passes over cells with smaller time steps. The aim is to provide a description of a controlled grid resolution approach in both space and time and to demonstrate its effectiveness for a selected class of problems. Refinement of grids is carried out whenever preselected differences exceed certain threshold limits. In general, the resolved grid field is itself unsteady, with rates of change that vary from large values during transients or unsteady flow to virtually zero for near steady-state solutions.

The algorithm periodically examines the evolving solution, applies spatial adaptation to the existing grid, determines an appropriate time-stepping sequence to make up consistent time-stride units for the entire domain, and finally integrates the equations. The spatial adaptation involves the detection of regions with large spatial nonuniformities and a subsequent subdivision of the corresponding grids. If spatial nonuniformities diminish later, return to a coarser mesh is allowed up to the initial coarsest grid. When the initial flowfield is itself nonuniform, consistent pre-embedding is applied while making certain that the grid division procedure does not introduce interpolation errors in the initial field. During the course of integration, temporal gradients are monitored so as to maintain time steps for adequate local resolution and stability. The time difference between two consecutive isotemporal surfaces is the maximum time step allocated to any cell and is referred to as a *time stride*.

Presented as Paper 88-0510 at the AIAA 26th Aerospace Sciences Meeting, Reno, NV, Jan. 11-14, 1988; received Jan. 25, 1988; revision received Dec. 15, 1988.

*Research Assistant (currently, Senior Scientist, Spectral Sciences Inc., Burlington, MA). Member AIAA.

†Professor, Department of Aeronautics and Astronautics. Associate Fellow AIAA.

Governing Equations

The conservation equations for two-dimensional reacting flow are

$$\frac{\partial U}{\partial t}+\frac{\partial F}{\partial x}+\frac{\partial G}{\partial y}=W \tag{1}$$

The state, flux, and source vectors are

$$U=(\rho,\rho u,\rho v,\epsilon,\rho Y_1,\ldots,\rho Y_S)^T$$

$$F=(\rho u,\rho u^2+p,\rho uv,u(\epsilon+p),\rho uY_1,\ldots,\rho uY_S)^T$$

$$G=(\rho v,\rho uv,\rho v^2+p,v(\epsilon+p),\rho vY_1,\ldots,\rho vY_S)^T$$

$$W=(0,0,0,0,\dot{W}_1,\ldots,\dot{W}_S)^T \tag{2}$$

where ρ, (u, v), ϵ, and p are the density, velocity components, total energy per unit volume, and pressure, respectively. The mass fraction of the sth species ($s = 1,\ldots,S$) is denoted by Y_s and $\dot{W}_s$ is the associated chemical source term. The vectors U, F, G, and W each have $4 + S$ components, but, since $\Sigma_{s=1}^{S} Y_s = 1$, only $S - 1$ species equations need be considered. The system is supplemented by the equations of state

$$p=\rho\Re T\sum_{s=1}^{S} Y_s/\hat{m}_s \tag{3}$$

$$\frac{\epsilon}{\rho}=\sum_{s=1}^{S} Y_s\left(H_{f_s}+\int_{T_0}^{T} C_{p_s}\,\mathrm{d}T\right)+\frac{u^2+v^2}{2}-\frac{p}{\rho} \tag{4}$$

where $\Re$, T, T_0, $\hat{m}_s$, H_{f_s}, and C_{p_s} are the universal gas constant, temperature, reference temperature, molecular mass, heat of formation, and constant-pressure specific heat, respectively. The system remains invariant in nondimensional form if the reference values are chosen as

$$t_r=L_r/u_r \qquad u_r^2=p_r/\rho_r=H_r=C_{p_r}T_r$$

$$T_r=\hat{m}_r p_r/\rho_r\Re \qquad \epsilon_r=p_r=\rho_r u_r^2$$

$$\dot{W}_r=\rho_r u_r/L_r \qquad \hat{m}_r=1/\textstyle\sum \frac{Y_{s_r}}{\hat{m}_s} \tag{5}$$

where subscript r denotes the reference values. However, the thermal equation of state becomes

$$p=\rho T\sum_{s=1}^{S}\frac{Y_s}{\hat{m}_s} \tag{6}$$

For R reactions of the form

$$\sum_{s=1}^{S} \alpha_{sr} A_s \rightleftharpoons \sum_{s=1}^{S} \beta_{sr} A_s, \qquad r = 1,\ldots,R \tag{7}$$

stiffness arises from the source terms

$$\frac{\dot{W}_s}{\hat{m}_s} = \sum_{r=1}^{R} (\beta_{sr} - \alpha_{sr}) \left[K_{fr} \prod_{l=1}^{S} \left(\frac{\rho Y_l}{\hat{m}_l} \right)^{\alpha_{lr}} - K_{br} \prod_{l=1}^{S} \left(\frac{\rho Y_l}{\hat{m}_l} \right)^{\beta_{lr}} \right] \tag{8}$$

The rate constants are assumed to be of the generalized Arrhenius form, e.g.,

$$K_{fr} = A_{fr} T^{\eta} \exp(-E_{fr}/T) \tag{9}$$

Integration Scheme

The integration basis is a generalization of a second order accurate Lax-Wendroff finite-volume scheme.[6] State, flux, and source vectors are stored at the nodes. The generalization introduces chemical source terms and spatiotemporal adaptation. Consider the physical domain cells A-D adjacent to node i in Fig. 1.

The *cell change* originates from a flux balance for cell C

$$\Delta U_C = \Delta t_C W_C + \frac{\Delta t_C}{A_C} \oint_C (F\,dy - G\,dx) \tag{10}$$

or

$$\begin{aligned} \frac{A_C}{\Delta t_C} \Delta U_C = {} & A_C W_C + F_W(y_l - y_i) - G_W(x_l - x_i) \\ & + F_N(y_k - y_l) - G_N(x_k - x_l) \\ & + F_E(y_j - y_k) - G_E(x_j - x_k) \\ & + F_S(y_i - y_j) - G_S(x_i - x_j) \end{aligned} \tag{11}$$

where A_C represents the cell area and subscripts S, E, N, W indicate the south, east, north, west fluxes; i.e., the F flux for the north and south faces are $F_N = (F_l + 2F_n + F_k)/4$ and $F_S = (F_i + F_j)/2$. Next, the contribution of the cell to its corner nodes is evaluated from the *distribution formulas*

$$\begin{aligned} \delta U_{iC} &= \tfrac{1}{4}\left(\Delta U - \frac{\Delta t}{A} \Delta \tilde{F} - \frac{\Delta t}{A} \Delta \tilde{G} + q \frac{\Delta t}{2} \Delta W + \Psi_i \right)_C \\ \delta U_{jC} &= \tfrac{1}{4}\left(\Delta U + \frac{\Delta t}{A} \Delta \tilde{F} - \frac{\Delta t}{A} \Delta \tilde{G} + q \frac{\Delta t}{2} \Delta W + \Psi_j \right)_C \\ \delta U_{kC} &= \tfrac{1}{4}\left(\Delta U + \frac{\Delta t}{A} \Delta \tilde{F} + \frac{\Delta t}{A} \Delta \tilde{G} + q \frac{\Delta t}{2} \Delta W + \Psi_k \right)_C \\ \delta U_{lC} &= \tfrac{1}{4}\left(\Delta U - \frac{\Delta t}{A} \Delta \tilde{F} + \frac{\Delta t}{A} \Delta \tilde{G} + q \frac{\Delta t}{2} \Delta W + \Psi_l \right)_C \end{aligned} \tag{12}$$

These distribution formulas allow for different time steps and cell volumes for cells adjoining a common node. The term Ψ incorporates the effect of artificial viscosity as described below. The flux and source changes are given by

$$\begin{aligned} \Delta \tilde{F} &= \left(y_\eta \frac{\partial F}{\partial U} - x_\eta \frac{\partial G}{\partial U} \right) \Delta U \equiv y_\eta \Delta F - x_\eta \Delta G \\ \Delta \tilde{G} &= \left(x_\xi \frac{\partial G}{\partial U} - y_\xi \frac{\partial F}{\partial U} \right) \Delta U \equiv x_\xi \Delta G - y_\xi \Delta F \\ \Delta W &= \frac{\partial W}{\partial U} \Delta U \end{aligned} \tag{13}$$

A typical example of a metric term for cell C is

$$y_\eta = \frac{y_n - y_s}{\Delta \eta} = \Delta y_{ns} = \frac{y_k + y_l - y_i - y_j}{2} \tag{14}$$

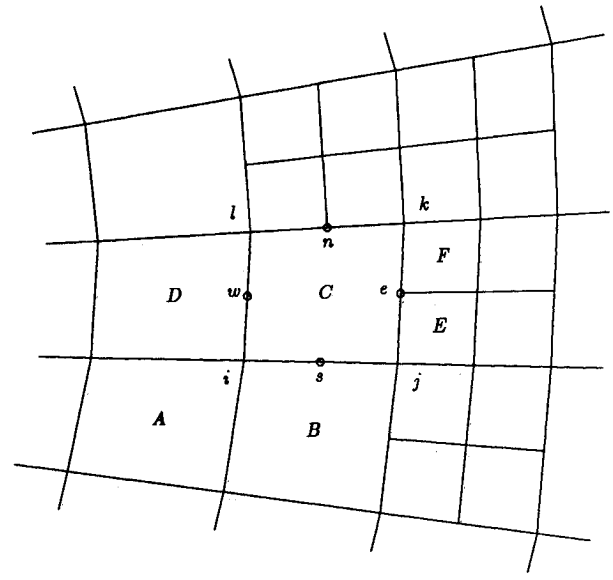

Fig. 1 Portion of physical grid.

The factor q appears in the distribution formulas so that assigned values of 0 or 1 will exclude or include a second-order source term. For a linearized source term model, a stability study[7] shows that no substantial gain in stability limits is acquired, over the explicit scheme, if the second-order source term is retained while treating the first-order source term implicitly. However, if only first-order implicit source terms are retained ($q = 0$), the stability becomes constrained solely by the familiar CFL condition. The remaining second-order flux terms are essential for stability and are always retained. The implicit source vector is useful when chemical reactions would otherwise impose severe time restrictions for stability, thereby making time steps minuscule compared to resolution requirements. Although implicit modeling may be advantageous in overcoming the reaction stability liminations, it is inappropriate when there are time-step constraints due to local rapid chemical adjustments. Of course, when interest is limited to the steady state, the implicit advantage can be fully utilized in bypassing the resolution requirements,[8-10] but only if it is clear that real gas behavior is independent of transient history.

Since an implicit source term for a cell C can be written as

$$W_C^{n+1} = W_C^n + \left. \frac{\partial W}{\partial U} \right|_C \Delta U_C \tag{15}$$

the implicit form of Eq. (10) becomes

$$\Delta U_C = \left(I - \frac{\partial W}{\partial U} \Delta t \right)_C^{-1} \left[\Delta t W^n + \frac{\Delta t}{A} \oint (F\,dy - G\,dx) \right]_C \tag{16}$$

This equation, instead of Eq. (10), is used in conjunction with the distribution formulas [Eq. (12) with $q = 0$] while looping over cells whenever the source implicit scheme is used.

The *cell change*, ΔU_C, must take into account the situation when cell C is adjacent to an interface as depicted in Fig. 1. While for cell C the nodes e and n actually exist, the nodes w and s are irrelevant; nevertheless, for the sake of a flux balance one can define, e.g., $F_w = (F_i + F_l)/2$. The distribution formulas are used to determine contributions to the corner nodes i, j, k, l when integrating C, whereas for midface nodes such as e a simple average, $\delta U_{eC} = (\delta U_j + \delta U_k)_C/2$, is used. The node e is treated in the usual manner [Eq. (12)] when integrating cells E and F in Fig. 1.

Artificial Viscosity

Artificial viscosity is needed to suppress odd-even decoupling modes associated with the integration scheme and dis-

persion effects adjacent to strong shocks. The dissipation is introduced only at corner nodes whenever integrating a particular cell. For example, its contribution in cell C to node i Fig. 1 is

$$\Psi_{iC} = \frac{\Delta t_C}{\Delta s_C}\left(\frac{\sigma_i U_i + \sigma_j U_j + \sigma_k U_k + \sigma_l U_l}{4} - \sigma_i U_i\right) \tag{17}$$

where $\Delta s_C = 2A_C/P_C$ with P_C being the perimeter. As shown in Ref. 7, this form results by considering a Laplacian type term for the artificial diffusion. The *viscosity* coefficients are stored at all nodes and have the form

$$\sigma_i = \sigma_{\min} + \frac{\delta}{4}(\kappa_A + \kappa_B + \kappa_C + \kappa_D) \tag{18}$$

where, for example, for a general cell C, the quantity κ_C depends upon a density switch

$$\kappa_C = \left|\frac{\rho_e - \rho_w}{\rho_e + \rho_w}\right| + \left|\frac{\rho_n - \rho_s}{\rho_n + \rho_s}\right| \tag{19}$$

The first or second differences of pressure are commonly used to scale the artificial viscosity coefficient. However, pressure is constant across contact surfaces and so density is used in the present work. For a midface node such as e, a lesser viscosity coefficient is needed and the viscous weight is accumulated only from cells whose corners include the node e, i.e., $\sigma_e = \sigma_{\min} + \delta(\kappa_E + \kappa_F)/4$. The constant δ is chosen so that $\sigma \in [\sigma_{\min}, \sigma_{\max}]$ typically between 0.05 and 0.5. The boundary nodes are adjusted to yield a reflection condition.

Spatial Adaptation

Spatial resolution is essential near features like shocks, relaxation zones, vortices, slip lines, etc., because a discrete model inherently spreads flow discontinuities over several cells and thereby degrades accuracy. Adaptive algorithms have the advantage that the meshes are refined only where necessary and as the solution evolves, thereby providing accurate and relatively inexpensive solutions.

One approach that detects flow features examines the first differences of a single-criteria variable.[1,5] The variations over the length scale of a mesh do provide a measure of the local numerical error; however, a single variable (e.g., density) may be insufficient when features in different regions are characterized by different time and length scales. For example, a contact surface may occur in one location with a small density gradient concurrently with a classical shock elsewhere without mass fraction gradients. Therefore, a multivariable approach is suggested; the type of differences used for spatial adaptation will be explained first.

Suppose density to be one of the components of a criteria variable vector Q. Since it is necessary to adapt frequently[4] for most unsteady flows, an efficient differencing scheme is of some importance. To minimize the computing time, only the corner vertices of a cell are considered when evaluating differences. For cell C in Fig. 1, the differences for $m = i, j, k, l$, are

$$\Delta\rho_m = \rho_C - \rho_m \text{ with } \rho_C = \frac{\rho_i + \rho_j + \rho_k + \rho_l}{4} \tag{20}$$

Next $\Delta\rho_{\max}$ and $\Delta\rho_{\min}$ are evaluated, which would be, for example, the maximum and minimum values for cell C over the nodes i, j, k, l. The cell difference $\Delta\rho_C$ is set according to the maximum if $|\Delta\rho_{\max}| > |\Delta\rho_{\min}|$ or to its minimum if $|\Delta\rho_{\max}| < |\Delta\rho_{\min}|$. When the values are equal, the cell change is assigned randomly to one of these. For a large number of cells, one may assume that the average of all such changes approximates zero, since there is equal likelihood for a cell to acquire positive or negative values. However, no such assumption is made here. We shall denote $\Delta\rho_C$ by q_1^C, indicating the first component of the spatial criteria vector Q and the mean value of all q_1^C by μ_1, which may be approximately zero. Once all elements of the vector Q are determined for each cell, the covariance matrix $\Sigma = \{s_{ab}\}$ follows from

$$s_{ab} = \sum_{c=1}^{N} \frac{1}{N}(q_a^c - \mu_a)(q_b^c - \mu_b) \tag{21}$$

where N is the total number of cells in the domain. To accelerate the adaptive process, one may assume that $s_{ab} = 0$ when $a \neq b$ for suitably chosen variables. A single scalar criteria variable then lumps the effects of the multivariable components of Q for each cell and has the form

$$r^2 = Q^T \Sigma^{-1} Q \tag{22}$$

This *refinement parameter* reduces to the familiar $r = (q - \mu)/\sqrt{s_{11}}$ form for a single-variable situation. One threshold value, $r_{1\max}$, is selected from the histogram records as the value corresponding to a specific fraction (usually 20%) of the cells for which $r > r_{1\max}$; a second one, $r_{2\max}$, is used to avoid cell division in globally uniform fields. A single threshold value, $r_{\max} = \max(r_{1\max}, r_{2\max})$, is then used as the decision basis for cell division. When $r_{1\max} > r_{2\max}$, all cells flagged for division actually may not be adapted. This occurs if the *spatial level* of the would be subcells pertaining to a marked cell exceeds some user-supplied maximum level (coarse cells are level 0, cells divided once are level 1, etc.). Furthermore, cells remain undivided if the difference between any two contiguous cell levels would otherwise exceed unity. A decision basis for cell merger $r_{\min}$ is set to about 20% of the resolution threshold value. When the associated refinement parameter diminishes on a previously refined grid and becomes less than the merger critical limit, those contiguous cells (which were derived from the same parent) may be fused. The cells are not merged if the difference in level between the parent cell and any of the neighbors would otherwise exceed unity. The coarsest global grid is never merged no matter how smooth the evolving solution proves to be.

Temporal Adaptation

Temporal and spatial adaptation procedures are applied separately. The spatial process is carried out at the current time level and all spatial locations, but infrequently relative to the number of temporal adaptations. Nevertheless, the frequency of spatial adaptations does depend upon the time rate of change of the flow feature being resolved. On the other hand, temporal adaptation is repeated after each time stride at all spatial locations and must anticipate subsequent changes in the flowfield as the features move. The four steps needed to complete a temporal grid adjustment are:

1) A determination of an allowable Δt for each cell.

2) Reassignment of Δt to be multiples (in powers of two) of the global minimum time step $\Delta t_{\min}$.

3) Further reassignment of Δt distributions such that adjacent cells vary at most by a factor of four.

4) Determination of a proper integration sequence over the cell domain.

The time step is subject to the CFL restriction[11]

$$\frac{\Delta t_{stb}}{\Gamma A_C} \leq \min\left(\frac{1}{|u\Delta y_{ns} - v\Delta x_{ns}| + a_f \mathfrak{D}_{ns}}, \frac{1}{|u\Delta y_{ew} - v\Delta x_{ew}| + a_f \mathfrak{D}_{ew}}\right) \tag{23}$$

where a_f is the local frozen speed of sound, Γ the CFL number, and $\mathfrak{D}^2 = \Delta x^2 + \Delta y^2$. In the presence of rapid adjustments, the more important resolution requirement Δt_{res} follows from a threshold criterion that is based on the maximum allowable change $\Delta U_{C_{\max}}$ for the *temporal criteria variable*; i.e.,

$$|\Delta U_C| \leq \Delta U_{C_{\max}} = \epsilon_1 |U_C| + \epsilon_0 \tag{24}$$

where the ϵ_i are small positive numbers. Effectively, the change is limited to a fraction of the state value of the temporal criteria variable excepting for vanishingly small levels. From Eq. (10), it follows that

$$\Delta t_{\text{res}} = \frac{|\epsilon_1 U_C + \epsilon_0| A_C}{A_C W_C + \oint_C (F\,dy - G\,dx)} \tag{25}$$

Since the resolution requirement Δt_{res} may or may not exceed the stability requirement Δt_{stb} the actual time step is

$$\Delta t_C = \min\{\Delta t_{\text{res}}, \Delta t_{\text{stb}}\} \tag{26}$$

A time constraint due to reaction kinetics does not appear here since the reacting flow computations were performed with source implicit modeling. For time accurate descriptions, a criterion such as Eq. (25) is desirable for both explicit and implicit integration schemes.

Based on Eq. (26), global minimum and maximum Δt can be determined for the spatial domain and the size m of the time stride may then be assigned such that

$$2^m \le \min\left\{\frac{\Delta t_{\max}}{\Delta t_{\min}}, 2^M\right\} < 2^{m+1} \tag{27}$$

Note that m is the *current maximum allowable temporal level* for domain cells and is constrained to be less than or equal to a prescribed maximum level M. Such a constraint on temporal levels is necessary to avoid very long time-stride units that may cause spillage of the feature being resolved from the spatially embedded region.[4] A flow feature generally implies an associated characteristic speed; the spatially embedded region must be sufficiently large to ensure that the feature will remain within the embedded region during the subsequent time stride. Hence, the embedded portion must be enlarged for moderate to large-sized time strides. Although temporal embedding involving long time strides helps to reduce CPU time, the increased number of extension nodes can be expensive and a balance between the two competing effects is necessary. Actual time steps for a given cell C are reassigned according to

$$\Delta t_C^{\text{new}} = 2^n \Delta t_{\min} \tag{28}$$

where the level $n \le m$ is given by

$$2^n \le \min\left\{\frac{\Delta t_C}{\Delta t_{\min}}, 2^m\right\} < 2^{n+1} \tag{29}$$

Another facet of temporal level stiffness is that time steps can vary appreciably for contiguous cells. This is improbable for frozen flows because a division into four subcells reduces the time step by a factor of two and hence this facet of temporal level stiffness can be avoided by controlling the difference of spatial level embedding between contiguous cells. For reacting cases, the source terms can vary appreciably between contiguous cells and hence can cause a corresponding variance of time steps. To avoid such occurrences, the cell time step is restricted to at most four times the minimum time step of the surrounding cells.

On completing all readjustments, cells with the same temporal levels are grouped together for subsequent integration. Thus cells with time steps $\Delta t_{\min}$ are in group level 0, those with $2\,\Delta t_{\min}$ are in group level 1, and so on. The total number of time steps needed for cells in level n to advance to the next time stride is 2^{m-n}.

The order in which the integration over the cells takes place is also important.[4] Successive integrations over the same cell in passing from one isotemporal surface to the next will produce a degraded solution, since information from neighboring cells is not allowed to propagate. A cycle of P_T integration passes completes a time-stride unit, the total number being $P_T = 2^{m+1} - 1$. On pass $P \in [1, P_T]$ cells with temporal level n are integrated if $(P - 2^n)/2^{n+1}$ is an integer.

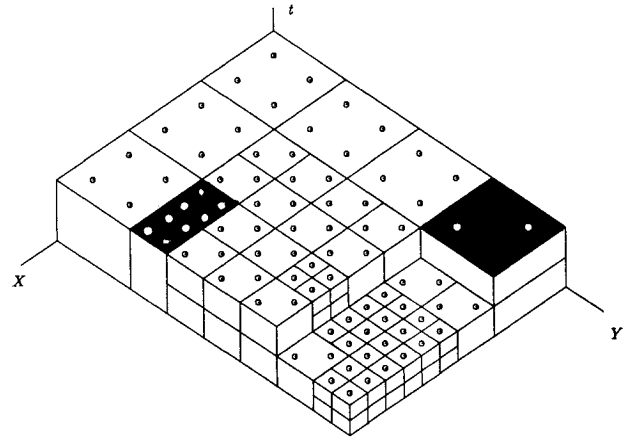

Fig. 2 Time stride with $m = 2$ for a portion of space/time grid.

Nodes at the boundary of cells with different time steps—*nodits*[4]—are not necessarily the same as middle nodes for spatial interfaces. No special formulation is needed at nodits and in order to render the actual spatial location of any temporal level cell irrelevant, a data base must be constructed so as to store cells at the same temporal level together. There is no such restriction for spatial adaptation pointers. The choice of such a data base allows the calculations for each pass to be performed in parallel; the data dependencies occur only at nodits between various passes for a given integration sequence. However, the integration order does not strictly have to follow the aforementioned sequence at nodits and such data dependencies will cause only slight variations between parallel and nonparallel calculations.

As an example consider the time stride in Fig. 2 with $M = 2$ as the prescribed maximum time level of cells. Also suppose that the time-step variation is such that the current maximum allowable temporal level of $m = 2$ is possible and, therefore, $P_T = 7$. For clarity, a slice has been removed from the figure. The dots on the top surfaces of each cell indicate the time step as a multiple of the global minimum time step. Hence, cells with one, two, and four dots are at levels $n = 0, 1, 2$. The chemical source terms may alter the time-step distributions in such a way as to create cells with spatial resolution in the absence of temporal resolution (cells with four dots and shaded top surfaces) and temporal resolution in the absence of spatial resolution (cells with two dots and shaded top surfaces). Such complications do not exist for frozen flow computations. The makeup of the time-stride changes with the movement of the flow features being resolved and a different number of levels may exist for consecutive time strides. The generation of fresh time strides depends, in fact, upon the velocity of the features; hence, for fast-moving features, time strides might be renewed after each spatial adaptation operation and vice versa.

Case Studies and Initial Conditions

Numerical experiments were carried out for a geometry consisting of a circular arc convex surface on the lower surface of a cascade configuration. On imposing a high pressure at the cascade entrance, a shock propagates to the right along the channel. This is initially a normal shock that later develops into a complex propagating shock pattern. The medium was taken to be either a perfect gas or a nonequilibrium Lighthill gas.

For a frozen flow, the conditions across the moving shock with shock Mach number M_f and ratio of specific heats γ are given by[12]

$$\frac{p_i}{p_e} = \frac{2\gamma}{\gamma+1} M_f^2 - \Gamma \qquad \frac{\rho_i}{\rho_e} = \frac{\Gamma + p_i/p_e}{1 + \Gamma p_i/p_e}$$

$$u_e = 0 \qquad u_i = \frac{2}{\gamma+1} a_e \left(\frac{M_f - 1}{M_f}\right) \tag{30}$$

where $\Gamma = (\gamma - 1)/(\gamma + 1)$, $a_e^2 = \gamma p_e/\rho_e$, and $()_i$, $()_e$ refer to inlet and exit.

For a reacting flow, the nonequilibrium source term for a Lighthill ideal dissociating gas, $Z_2 \rightleftharpoons 2Z$, is[13]

$$\dot{W}_Z = \Phi T^{\eta}\rho\left[(1 - Y_Z)e^{-\theta_D/T} - \frac{\rho}{\rho_D}Y_Z^2\right] \tag{31}$$

with the nondimensional reaction parameter given by

$$\Phi = \frac{C_f T_r^{\eta}\rho_r L_r}{\dot{m}_Z\sqrt{p_r/\rho_r}} \tag{32}$$

where C_f, η, θ_D, and ρ_D are physical constants and subscript r denotes reference quantities. In contrast to the frozen case, a partially dispersed shock involves a frozen jump (station e to f), followed by a relaxation tail (station f to i) that is characterized by a gradual adjustment to equilibrium on the downstream side, $()_i$, of the shock. This dispersed behavior served as the initial conditions for all finite-rate cases. The overall change between stations e and i is given by equilibrium shock relations.[13]

Denoting the mass fraction of dissociated atoms at station k by Y_k, the *frozen* shock Mach number is given by

$$M_f^2 = \frac{u_f^2}{\gamma_e p_e/\rho_e} \text{ with } \gamma_e = \frac{4 + Y_e}{3} \tag{33}$$

The differential equation for the mass fraction in the relaxation zone is

$$\frac{dY}{dx} = \Phi T^{\eta}\frac{\rho}{w}\left[(1 - Y)e^{-\theta_D/T} - \frac{\rho}{\rho_D}Y^2\right] \tag{34}$$

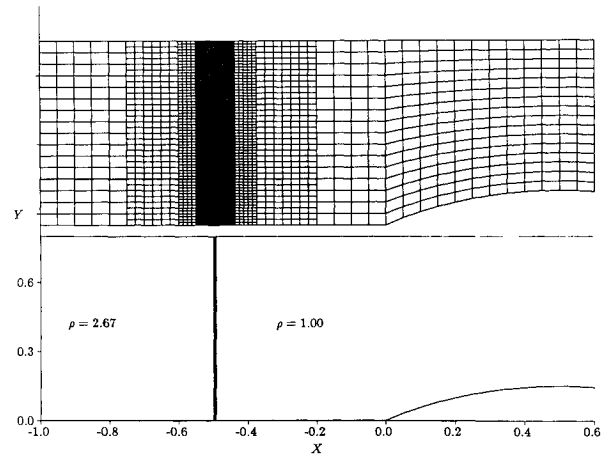

Fig. 3 Grid and density contours at $t = 0$ for frozen flow, $M_f = 2$, $\gamma = 1.4$.

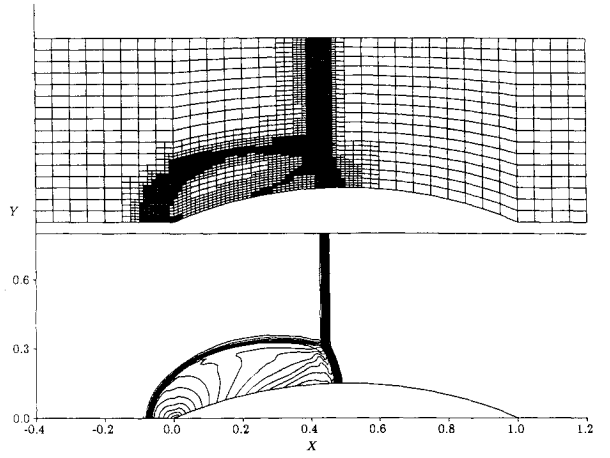

Fig. 4 Grid and density contours at $t = 0.4$ for frozen flow, $M_f = 2$, $\gamma = 1.4$.

where w is the fluid velocity in a frame of reference attached to the frontal shock. Starting from an initial frontal shock location ($x = x_f$ at $t = 0$) with $Y = Y_f = Y_e$, the other quantities at station f are given by the *frozen* shock relations between stations f and e for the normal (frontal) shock. The usual integral conservation relations connecting state f and any position inside the relaxation zone can be used to define the density, pressure, and velocity in terms of the atom mass fraction and, as such, the differential equation can be integrated. Once velocities w in the stationary shock frame are known, the velocities u in the moving shock frame flow from $u = w_e - w$. A relaxation length x_t may be defined as the distance between the shock discontinuity at f and, where dissociation reaches 0.99, of the equilibrium value Y_i and is a convenient measure of the nonequilibrium scale between its zero (equilibrium) and infinite (frozen) limits.

Results and Discussion

Frozen Case

The first example was for a frozen medium ($\gamma = 1.4$) and a shock propagating at $M_f = 2$ past a 15% circular arc section as shown in Figs. 3-6 corresponding to the time periods of $t = 0$, 0.4, 0.8, and 1.2, respectively. The channel dimensions are normalized by the chord length and is spanned by $x \in (-1, 2)$, $y \in (0, 0.8)$. Other fluid properties are normalized with those of the quiescent gas. The shock is initially $t = 0$ at $x = -0.5$. The figures show both density contours and the corresponding spatial grids at the indicated time intervals. Clearly, the evolving spatial grid tracks the salient features. Three levels of spatial embedding beyond the base grid (16×60 cells) and four levels of temporal strides were used. Since the maximum eigenvalue ($u + a$) changes significantly across a moving shock, it is appropriate to use additional levels for temporal adaptation compared to those for spatial adaptation. The corresponding globally fine spatial grid has 4^3 as many cells and four levels of temporal strides imply 2^4 smallest time steps in each time stride. Hence, the space/time globally fine grid is expected to consume a factor of 1024 more CPU time than the globally coarse grid. The grid actually was uniformly pre-embedded by six cells and to three levels at $t = 0$ on both sides of the shock as shown in Fig. 3.

The unnecessarily fine region generated by pre-embedding to the left of the initial shock reverts back to the coarse grid as soon as the *usual* spatial adaptation process is turned on. A density refinement criterion was used with $r_{2\max} = 1.2$. Spatial adaptation was performed after each time-stride unit and the spatially adapted grid was arbitrarily extended by two additional cells on each side. The same values were used for the dissociating flow cases. At about $t = 0.2$, the shock reaches the leading edge of the arc and soon after a compression wave ensues from the bump, which then propagates upstream. The compression region strengthens and develops into a shock wave that propagates against the flow stream. The Mach number in the inlet region following the initial shock is $M_i = 0.96$ or equivalently a velocity of $u_i = 1.48$. The velocity of the near-normal shock moving back toward the entrance along the lower wall is $u = -0.36$ or $M = 1.20$ in a frame of reference attached to the front shock and with respect to the inlet sound speed.

At $t = 0.4$ (Fig. 4), the original frontal shock has traversed about 50% of the chord. The shock wave ensuing from the bump has interacted with the frontal shock to form a lambda shock structure. There is some evidence of a slip line emanating from the triple point, both from the density contours and the embedded grids. Since density sensors are used in the artificial viscosity formulation, it is reasonable to expect that the slip line would be appropriately captured. However, unless extremely fine cells are used, capturing of slip lines is a severe task for computations based on the conservation law form. The triple point moves vertically upward as the frontal shock moves downstream.

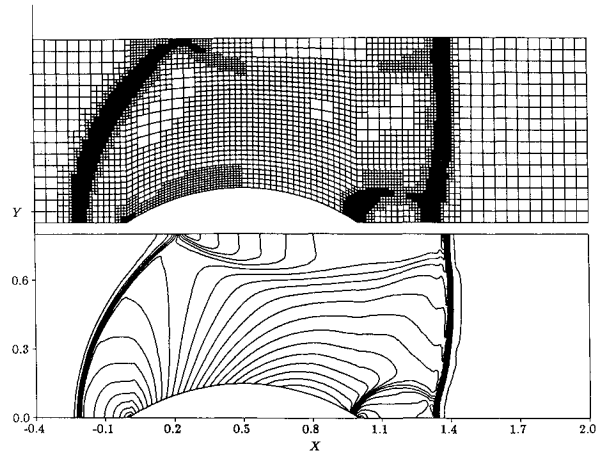

Fig. 5 Grid and density contours at $t = 0.8$ for frozen flow, $M_f = 2$, $\gamma = 1.4$.

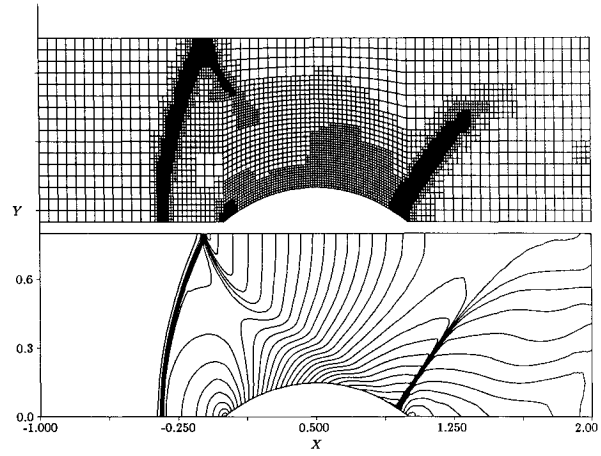

Fig. 6 Grid and density contours at $t = 1.2$ for frozen flow, $M_f = 2$, $\gamma = 1.4$.

Corresponding to $t = 0.8$, Fig. 5 shows the frontal shock arriving downstream of the bump surface and the rearward-facing shock developing a strong reflection from the upper boundary. The beginning of a secondary shock surface is apparent near the trailing edge of the section.

Finally, Fig. 6 shows the situation at $t = 1.2$ after the frontal shock has left the computational domain. A nonreflective boundary condition had been applied at the exit. Both the reflected bow shock of the upstream-facing front and the shock that originated near the trailing edge are now strengthening and moving upstream.

A similar frozen case has been studied by Yang et al.[14] Figure 7 compares their pressure contours for a globally fine grid at a time when the lower leg of the frontal shock is virtually at the trailing edge. This corresponds to $t = 0.65$ for the present case. Figures 8 and 9 indicate comparisons on the lower channel wall and at $y = 0.5$, the symbols represent interpolated data from Fig. 7 in Ref. 14. The agreement between the two solutions is considered reasonable.

Figure 10 shows the density distributions along the lower channel wall at various time stations. The vertical scale corresponds to the initial condition $t = 0$ and all the other curves are displaced by the vertical offset of 0.8.

Reacting Case

A second example used a Lighthill dissociating gas flowing over the same 15% circular arc bump. Constants for the Lighthill model for oxygen are $\eta = 0$, $\theta_D = 59{,}500$ K, $\rho_D = 150{,}000$ kg/m^3. Inlet temperature and density were chosen so

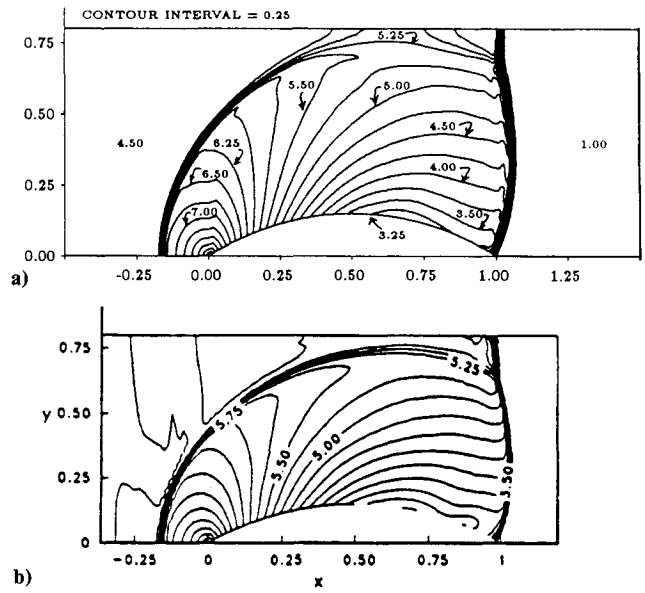

Fig. 7 Pressure contours at $t = 0.65$ for frozen flow, $M_f = 2$, $\gamma = 1.4$; a) present adaptive calculation, b) Ref. 14.

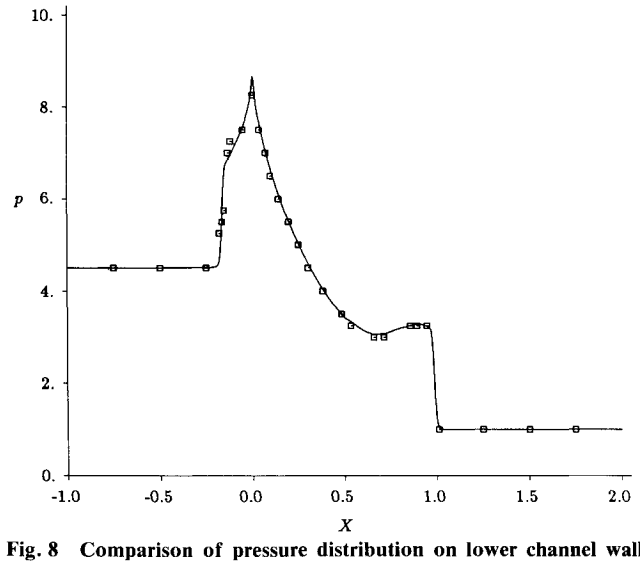

Fig. 8 Comparison of pressure distribution on lower channel wall for frozen flow (symbols represent data from Ref. 14).

as to yield 40% dissociated oxygen atoms under equilibrium conditions. The conditions at inlet and exit are

	T, K	ρ, kg/m^3	Y
Inlet, $(\,)_i$	5000	3.820	0.400
Exit, $(\,)_e$	4125	1.004	0.247

This corresponds to a shock moving through the channel at $M_f = 2$. The exit conditions are also the reference values for both the frozen and reacting cases. Note that the degree of dissociation at the exit corresponds to $\gamma = 1.417$ for comparison with the previous frozen case. Although the shock Mach number is identical in the two cases, the temperature, density, and pressure ratios are very different; i.e., for the reacting case the ratios are 1.212, 3.803, and 5.174, whereas those for the frozen flow are 1.688, 2.667, and 4.500, respectively. A choice of reaction parameter $\Phi = 10^4$ implies the relaxation length to be $x_r = 0.273$ times chord length.

By comparing Figs. 3 and 11, it can be seen that the pre-embedded grid at $t = 0$ spans a larger domain due to gradients in the relaxation zone trailing the frontal shock. The base grid

is again 16×60 with allowance for three spatial refinements and advancement by five temporal stages. The refinement parameter was based on density and mass fraction of atoms with $r_{2\max} = 1.2$.

Figure 12 shows density contours and the associated spatial grid at $t = 0.6$. The embedded grid is again seen to be capturing the salient features. The motivation for showing spatial grids as well as line contours has been to demonstrate the grid tracking capability for all of the necessary features without the introduction of spurious oscillations in the solution. If only density is used as a refinement parameter, the spatial adaptation fails to resolve the relaxation tail. However, a combination of density and atom mass fraction does yield satisfactory resolution of both the frontal shock and the relaxation zone. Figure 13 shows the distribution of the spatial variations of density and atom mass fraction for the spatial grid at $t = 0.6$ on *standardized scales* that allow for an unbiased spread of data. The numerical values of the averages μ_j were about seven orders of magnitude smaller than the (diagonal) standard deviations. Each square on the figure represents a single cell in the domain, which total 8508 at that time. The cells with large variations correspond to the data outside the *divide threshold ellipse* and are the cells marked for possible division. The fact that the ellipse has small eccentricity implies that the correlation between the two variations is relatively small for the type of differences chosen. The threshold ellipse corresponds to $r_{\max} = r_{1\max} = 1.8$ and is the locus of the points satisfying Eq. (22) with $r = r_{\max}$. The cells falling within the *collapse threshold ellipse* are marked for possible merger. About 70% of the cells lying between the two ellipses remain unaffected.

The contours of density and atom mass fraction are shown in Figs. 14 and 15 for several time stations. The time history of this case can also be examined by observing the distributions of density and atom mass fraction along the lower channel wall as shown in Figs. 16 and 17. The flow development is quite comparable to the previous frozen flow case. The reverse moving shock is much stronger compared to the frozen flow case, which moves at a speed of $u = -0.1$ or a Mach number of 1.31 based upon the undisturbed inlet sound speed and a frame of reference attached to it. The Mach number of the inlet stream itself is $M_i = 1.24$, which is supersonic compared to the previous case. The shock originating near the trailing edge remains at the same location, unlike the frozen flow case.

CPU Time Comparison

In order to assess the effectiveness of the spatiotemporal adaptive algorithm, calculations have been carried out on coarse, adapted, and fine grids between the time stations $t = 0$ and 0.3 for the frozen flow. In order to further curtail the overhead for the globally fine grid, the spatial domain was reduced to span $x \in (-0.6, 0.4)$ and $y \in (0, 0.6)$. The omitted spatial domain corresponded to regions that were either undisturbed or in the vicinity of the normal shock for $t \in (0, 0.3)$. The base grid resolution was kept the same as the previous two cases. The coarse grid corresponds to the base grid of the adapted case. Three spatial levels of embedding and four temporal stages were again allowed for the adapted case. The

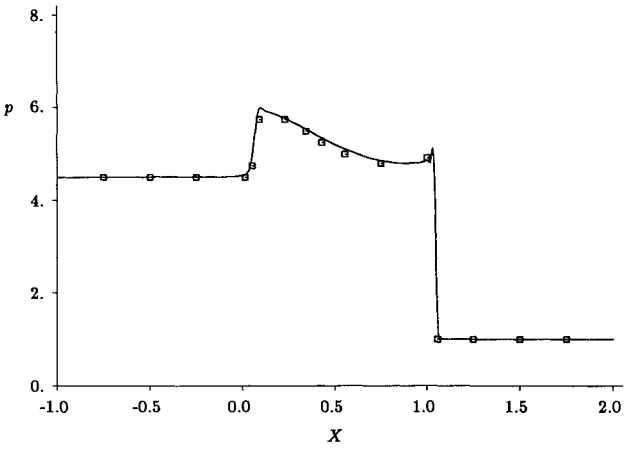

Fig. 9 Comparison of pressure distribution at $y = 0.5$ for frozen flow (symbols represent data from Ref. 14).

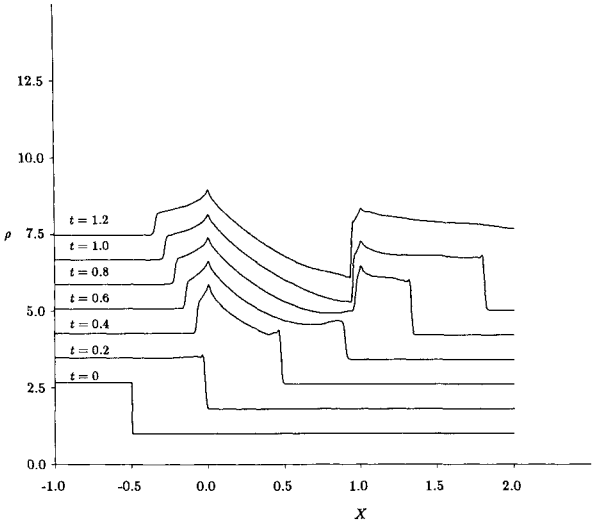

Fig. 10 Density profiles at the lower channel wall for frozen flow over a 15% circular arc, $M_f = 2$.

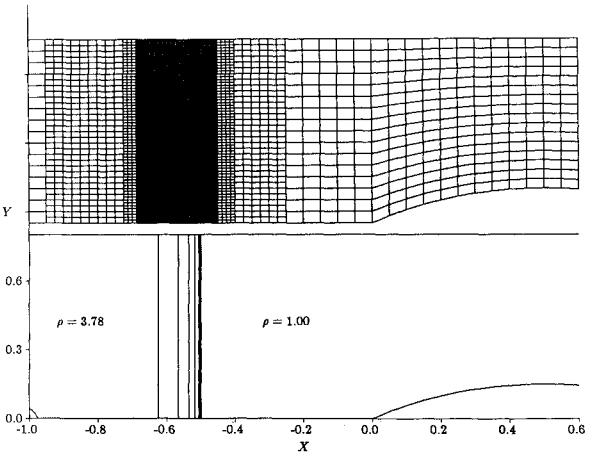

Fig. 11 Grid and density contours at $t = 0$ for dissociating oxygen flow over a 15% circular arc, $M_f = 2$, $\Phi = 10^4$.

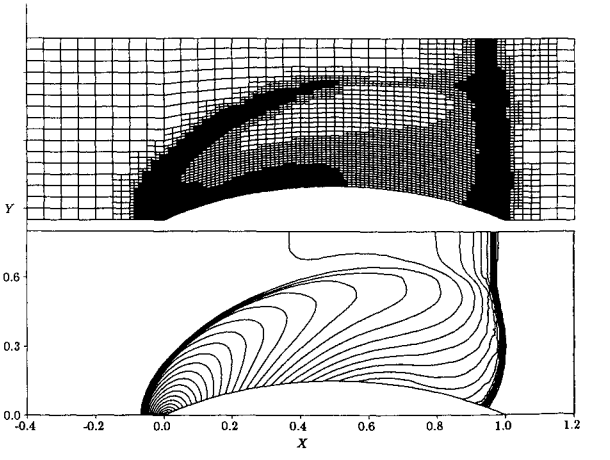

Fig. 12 Grid and density contours at $t = 0.6$ for dissociating oxygen flow over a 15% circular arc, $M_f = 2$, $\Phi = 10^4$.

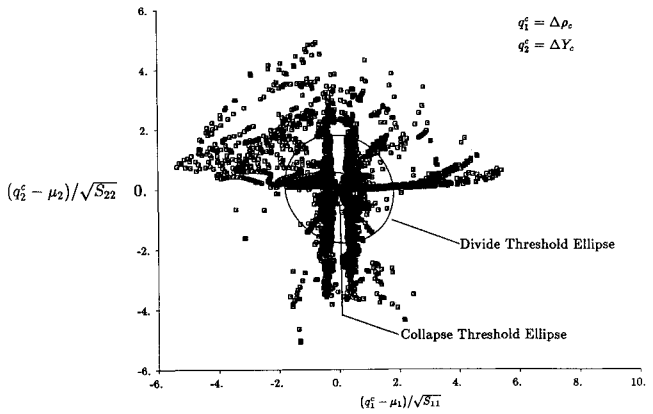

Fig. 13 Distribution of variations for spatial adaptation at $t = 0.6$ over a 15% circular arc, $M_f = 2$, $\Phi = 10^4$.

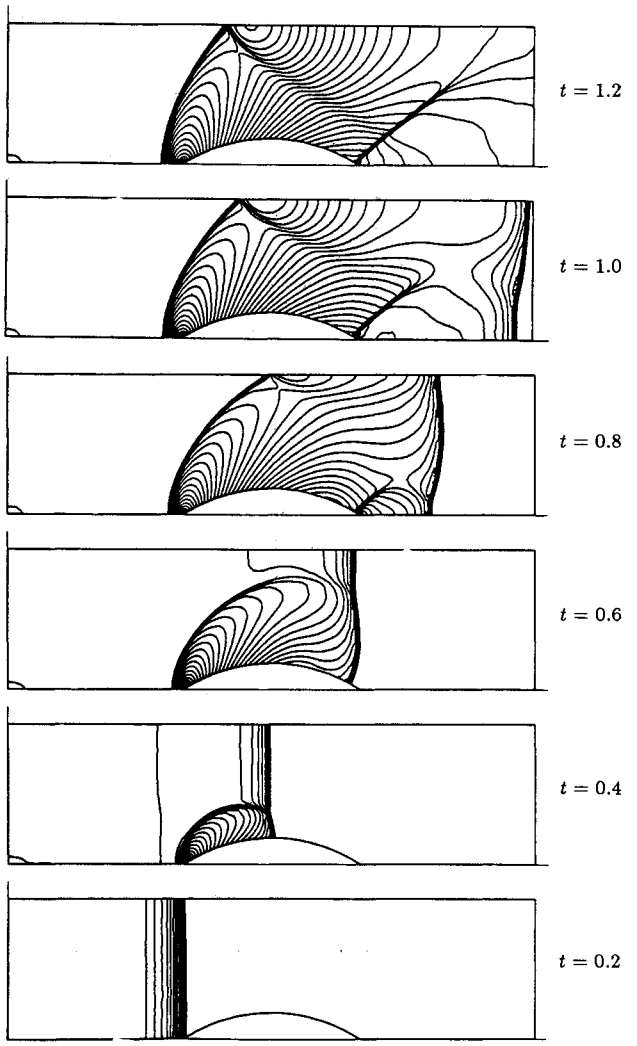

Fig. 14 Density contours for dissociating oxygen flow over a 15% circular arc, $M_f = 2$, $\Phi = 10^4$.

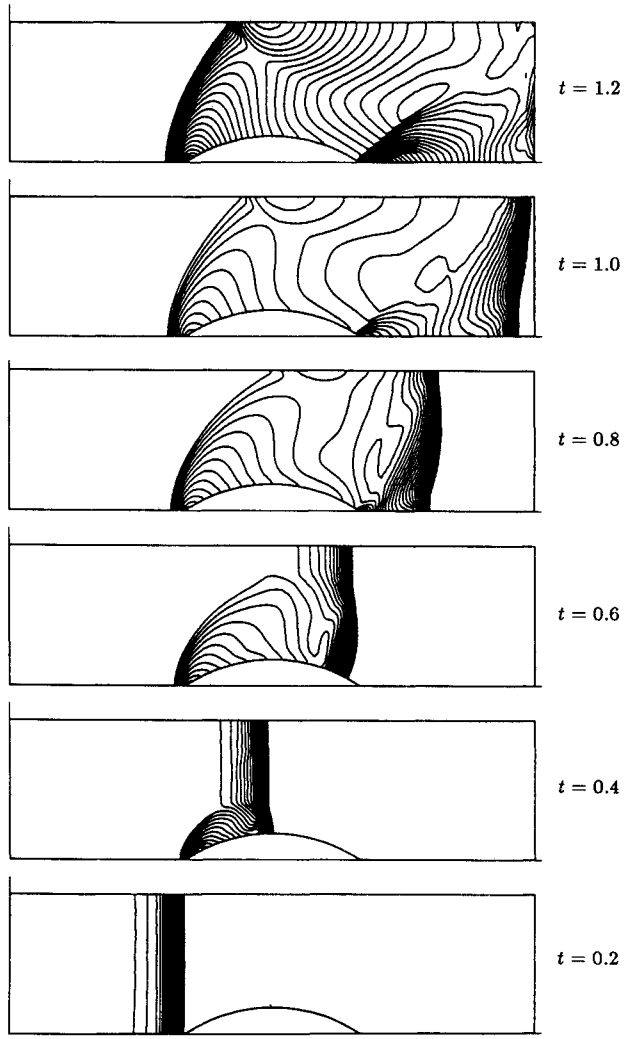

Fig. 15 Atom mass fraction contours for dissociating oxygen flow over a 15% circular arc, $M_f = 2$, $\Phi = 10^4$.

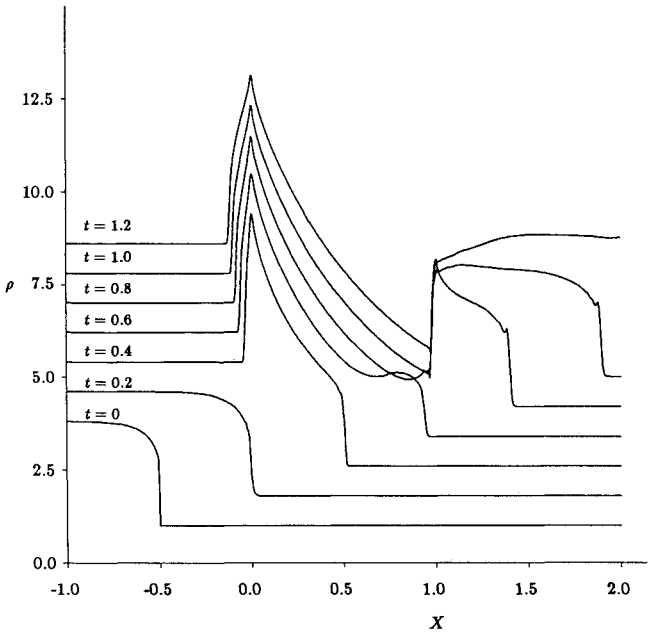

Fig. 16 Density profiles at the lower channel wall for dissociating flow over a 15% circular arc, $M_f = 2$.

global fine grid corresponds to the finest spatial level of the adapted case. Both fine and coarse grid solutions were carried out with a global minimum time step. Since the proportion of the adapted region to the overall computational domain is larger for a curtailed domain, the CPU gains can be inferred to be somewhat modest compared to the previous calculations. Nevertheless, the conservative results do provide reasonable justification for an adaptive approach in both space and time. The density contours at the final time of $t = 0.3$ for coarse, adapted, and fine grids are shown in Fig. 18 along with the adapted spatial grid.

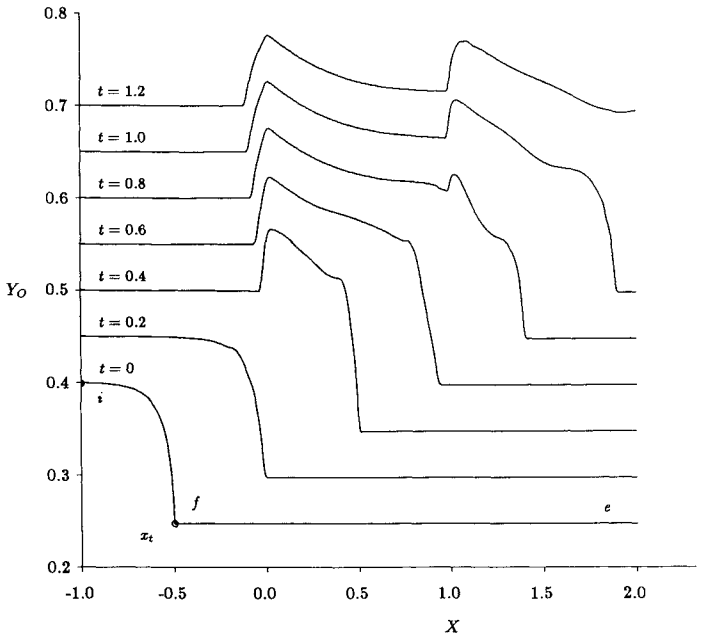

Fig. 17 Atom mass fraction distributions at the lower channel wall for 15% circular arc, $M_f = 2$.

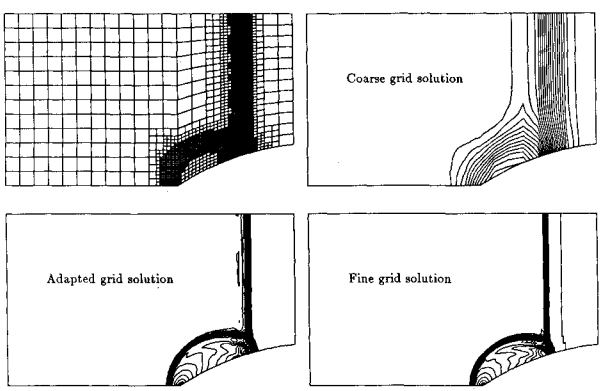

Fig. 18 Density contours at $t = 0.3$ for coarse, adapted, and fine grids for frozen flow over 15% circular arc, $M_f = 2$, $\gamma = 1.4$.

The calculation on the coarse grid took 51.0 s on a Micro-Vax II machine, of which 31.5 s were devoted to actual integration. For this coarse grid calculation, the initialization and output dump procedures consumed a significant fraction of the overall time. The corresponding fractions for initialization and output dump for adapted (about 1%) and fine (about 0.2%) grids were very small. The fine grid solution required a factor of 571.3 longer compared to the coarse grid integration time (or a factor of 352.5 for total time). The corresponding factors for the adapted grid were 26.3 based upon integration time and 16.7 based upon total time for the coarse grid. Hence, we estimate the spatiotemporal algorithm to be conservatively about an order of magnitude faster when compared to the globally fine approach for the frozen test example.

It is evident that a coarse grid solution is incapable of delineating features such as a shock wave, triple point, or slip line. However, the adaptive grid procedure does provide results comparable to those for a globally fine grid and at a fraction of the cost for the latter.

The effectiveness of the adaptive algorithm increases further when temporal resolution becomes essential in tracking local rapid chemical adjustments. Since adapted grid solutions for the completed dissociating cases prove to be longer by a factor of about seven than corresponding frozen flow cases, it was impractical to consider reacting, globally fine grid comparisons. Such reactive examples involve larger CPU times because of the additional (species) equations and refinement parameters. However, the dominant and potentially very stringent requirement is temporal resolution.

Conclusions

A strategy for automatic spatial and temporal grid embedding has been developed for inviscid two-dimensional reacting flows. The algorithm yields fair grid tracking of flow features and reasonably smooth interface behavior. The procedure has been shown to be effective in reducing CPU time, while retaining accuracy comparable to a globally fine solution. The algorithm becomes increasingly beneficial as temporal resolution requirements become locally more stringent.

Acknowledgment

This work was supported by NASA under Grant NAG-1-507, technical monitor N. Duane Melson.

References

[1]Dannenhoffer, J. F. and Baron, J. R., "Adaptive Procedure for Steady State Solution of Hyperbolic Equations," AIAA Paper 84-0005, Jan. 1984.

[2]Löhner, R., Morgan, K., Peraire, J., and Zienkiewicz, O. C., "Finite Element Methods for High Speed Flows," AIAA Paper 85-1531, July 1985.

[3]Oden, J. T., Strouboulis, T., and Devloo, P., "An Adaptive Finite Element Strategy for Complex Flow Problems," AIAA Paper 87-0557, Jan. 1987.

[4]Pervaiz, M. M. and Baron, J. R., "Temporal and Spatial Adaptive Algorithm for Reacting Flow," *Communications in Applied Numerical Methods,* Vol. 4, Jan. 1988, pp. 97-111.

[5]Shapiro, R. A. and Murman, E. M., "Cartesian Grid Finite Element Solutions to the Euler Equations," AIAA Paper 87-0559, Jan. 1987.

[6]Ni, R.-H., "A Multiple Grid Scheme for Solving the Euler Equations," *AIAA Journal,* Vol. 20, Nov. 1982, pp. 1565-1571.

[7]Pervaiz, M. M., "Spatio-temporal Adaptive Algorithm for Reacting Flows," Ph. D. Thesis, Dept. of Aeronautics and Astronautics, Massachusetts Institute of Technology, Cambridge, MA, April 1988.

[8]Bussing, T. E. and Murman, E. M., "A Finite Volume Method for Calculation of Compressible Chemically Reacting Flows," AIAA Paper 85-0331, Jan. 1985.

[9]Drummond, J. P., Hussaini, M. Y., and Zang, T. A., "Spectral Methods for Modeling Supersonic Chemically Reacting Flowfields," *AIAA Journal,* Vol. 24, Sept. 1986, pp. 1461-1467.

[10]Rivard, W. C., Farmer, O. A., and Butler, T. D., "RICE: A Computer Program for Multicomponent Chemically Reactive Flows at All Speeds," Los Alamos Scientific Laboratory, Los Alamos, NM, Rept. LA-5812, March 1975.

[11]Usab, W. J., "Embedded Mesh Solutions of the Euler Equation Using a Multiple-grid Method," Ph. D. Thesis, Dept. of Aeronautics and Astronautics, Massachusetts Institute of Technology, Cambridge, MA, Dec. 1983.

[12]Liepmann, H. W. and Roshko, A., *Elements of Gas Dynamics,* Wiley, New York, 1957.

[13]Vincenti, G. and Kruger, C., *Introduction to Physical Gas Dynamics,* Wiley, New York, 1965.

[14]Yang, J. Y., Lombard, C. K., and Bershader, D., "Numerical Simulation of Transient Inviscid Shock Tube Flows," *AIAA Journal,* Vol. 25, Feb. 1987, pp. 245-251.